Catalysis Science & Technology

ROYAL SOCIETY OF CHEMISTRY

PAPER

View Article Online
View Journal | View Issue

Cite this: *Catal. Sci. Technol.*, 2026, **16**, 1371

Synergistic effects of oxygen vacancies and the Schottky junction in Ni/CeNiO$_{3-x}$ catalysts for photothermal CO$_2$ methanation

Wenjing Tian,[ab] Nan Wang,*[ab] Wenxia Yan,[a] Ruixin Fu,[a] Teng Li[a] and Feng Yu *[ac]

Received 24th November 2025,
Accepted 25th December 2025

DOI: 10.1039/d5cy01413a

rsc.li/catalysis

In response to the increasingly severe pressure for CO_2 emission reduction, the development of efficient, low-temperature CO_2 conversion technologies is of great significance. This study focuses on the serious carrier recombination issue in photothermal catalytic CO_2 methanation and innovatively constructs Ni/CeNiO$_3$ and Ni/CeNiO$_{3-x}$ catalysts with different oxygen vacancy concentrations by regulating the oxygen vacancy concentration in CeNiO$_3$ precursors. The results show that under 250 °C photothermal conditions, Ni/CeNiO$_{3-x}$ achieves a CO_2 conversion rate of 91.2% and CH_4 selectivity of 93.1%, with a methane production rate of 163.7 mmol g^{-1} h^{-1}, significantly outperforming the Ni/CeNiO$_3$ reference catalyst. Mechanistic studies reveal that the Schottky junction at the Ni–CeO_2 interface promotes directional migration of photogenerated electrons and suppresses their recombination, while the abundant oxygen vacancies provide increased electron trapping capacity, thereby functioning to enhance CO_2 adsorption and activation on the material surface. The synergistic effect of these two factors significantly improves the photothermal catalytic performance. This study provides new insights for designing efficient and stable Schottky junction photothermal catalysts.

Introduction

Photo-assisted thermal catalytic CO_2 hydrogenation is an effective approach for converting CO_2 emissions from fossil fuels into CH_4, demonstrating broad application prospects.[1–6] As a clean energy source, CH_4 possesses a high heating value and is widely used in urban gas supply, power-to-gas systems, and CO_2 removal in spacecraft, among other fields.[7–9] However, the CO_2 molecule exhibits high thermodynamic stability and kinetic inertness due to its stable octet electron structure. The bond-breaking process requires overcoming a significant energy barrier, leading to limited kinetics for CO_2 reduction reactions at low temperatures. Utilizing solar energy for photo-assisted thermal catalysis can significantly reduce the reaction activation barrier, thereby enabling effective activation of CO_2 under mild conditions.[10–13] Nevertheless, catalysts currently still face the challenge of severe recombination of photogenerated carriers in practical applications, which limits the efficiency of CH_4 generation and catalytic stability.[14]

Therefore, developing photothermal catalysts that can effectively suppress carrier recombination and promote electron transfer is of great significance. In recent years, to improve solar energy utilization efficiency and catalytic performance, researchers have widely adopted the strategy of constructing Schottky junctions. This structure can regulate carrier migration behavior at the photocatalytic interface, effectively inhibiting the recombination of electron–hole pairs, thereby enhancing photocatalytic activity.[15] Additionally, introducing vacancy defects as electron trapping centers can further enhance the separation efficiency of photogenerated carriers and optimize catalytic performance.[10] For example, Guo *et al.*[16] introduced oxygen vacancies into $NiCo_2O_4$ *via* $NaBH_4$ treatment and constructed a Schottky heterojunction by compositing it with ZnCdS. The presence of oxygen vacancies significantly improved the material's conductivity, optimized the charge transfer pathway, and consequently accelerated the surface catalytic reaction kinetics. The Schottky junction enables electrons to migrate only in a single direction, thereby efficiently promoting electron transfer and enhancing photocatalytic hydrogen evolution performance. Sun *et al.*[17] successfully prepared a three-dimensional hierarchical hollow Bi/Bi_4Ti_{13}-O_{12} Schottky junction photocatalyst with tunable surface oxygen vacancies *via* a hydrothermal–solvothermal method.

[a] *Key Laboratory for Green Processing of Chemical Engineering of Xinjiang Bingtuan, School of Chemistry and Chemical Engineering, Shihezi University, Shihezi 832003, China. E-mail: nanwangsearl@outlook.com, yufeng05@mail.ipc.ac.cn*

[b] *Instituto de Investigaciones en Materiales, Universidad Nacional Autónoma de México, Circuito exterior s/n, Ciudad Universitaria, Del. Coyoacán, Ciudad de México, CP 04510, Mexico*

[c] *Carbon Neutralization and Clean Energy Technology Laboratory (CN&CE Tech Lab), Shihezi University, Shihezi 832003, China*

Leveraging the synergistic effect between the surface oxygen vacancies and the Schottky junction at the $Bi/Bi_4Ti_{13}O_{12}$ interface, this material significantly enhanced the capture and migration efficiency of photogenerated carriers while promoting the unidirectional electron transfer from $Bi/Bi_4Ti_{13}O_{12}$ to metallic Bi nanoparticles, achieving a highly efficient solar-driven nitrogen fixation reaction. Although existing studies have revealed that the synergistic effect between vacancy defects and Schottky junctions helps improve photocatalytic performance, their specific mechanism in the photothermal catalytic conversion of CO_2 still lacks systematic explanation.

This study utilizes $CeNiO_3$ as a structural precursor and constructs a $Ni/CeNiO_{3-x}$ catalyst through a two-step reduction strategy. The $Ni/CeNiO_{3-x}$ catalyst, further modulated by $NaBH_4$-induced oxygen vacancies, exhibits stronger electron coupling and enhanced CO_2 adsorption–activation capacity at the $Ni–CeO_{2-x}$ interface. The Schottky junction formed at the interface between Ni and the CeO_2 support effectively suppresses the recombination of photogenerated charges, enabling the $Ni/CeNiO_{3-x}$ catalyst to achieve 91.2% CO_2 conversion and 93.1% CH_4 selectivity under photothermal conditions at 250 °C. Through systematic structural and performance analysis, this study reveals that the synergistic effect between the oxygen vacancy concentration and the Schottky junction significantly enhances the spatial separation efficiency of photogenerated carriers, thereby accelerating the reaction kinetics of photothermal catalytic CO_2 hydrogenation to CH_4. This provides a new design strategy for efficient CO_2 resource utilization and the precise structural regulation of photothermal catalysts.

Experimental section

Catalyst preparation

The $Ni/CeNiO_3$ catalyst was prepared using a sol–gel method followed by H_2 reduction treatment. Firstly, 11.2 mmol of $Ni(NO_3)_2{\cdot}6H_2O$ (Analytical Reagent, Macklin, China), 11.2 mmol of $Ce(NO_3)_3{\cdot}6H_2O$ (Analytical Reagent, Macklin, China), and 22.4 mmol of citric acid (Analytical Reagent, Macklin, China) were dissolved in 70 mL of deionized water. The mixture was stirred continuously in an oil bath at 85 °C until a gel formed. The resulting gel was dried at 110 °C for 12 hours to obtain a loose solid, which was ground and then calcined in a muffle furnace using a two-stage program: first heated to 275 °C and held for 1 hour, then further heated to 600 °C and calcined for 6 hours, yielding the $CeNiO_3$ precursor. This $CeNiO_3$ precursor was reduced in a H_2 atmosphere for 2 hours to obtain the $Ni/CeNiO_3$ catalyst. The $Ni/CeNiO_{3-x}$ catalyst was prepared using a method involving $NaBH_4$ and subsequent H_2 reduction. Firstly, 0.38 g of $NaBH_4$ (Analytical Reagent, Guangdong Wengjiang Chemical Reagent Co., Ltd., China) was dissolved in 10 mL of deionized water to form a solution. This solution was added dropwise under stirring into 300 mL of an aqueous suspension containing 0.4 g of $CeNiO_3$. After the addition was complete, stirring was paused, and the system was diluted with distilled water to a total volume of 400 mL, followed by continuous stirring for 2 hours. After the reaction, the solid was collected by filtration and vacuum-dried at 60 °C for 12 hours, yielding the intermediate product $CeNiO_{3-1}$. Finally, $CeNiO_{3-1}$ was reduced again in a H_2 atmosphere for 2 hours to produce the catalyst $Ni/CeNiO_{3-x}$.

Catalyst characterization

The crystal structure of the materials was characterized by X-ray diffraction (XRD) using a Bruker D8 Advance diffractometer with Cu Kα radiation (λ = 0.154 nm). Morphology and microstructure information were obtained by scanning electron microscopy (SEM, Hitachi SU8020) and transmission electron microscopy (TEM and high-resolution TEM HRTEM, Tecnai G2 F30), respectively. Surface elemental distribution was analyzed using an X-ray energy dispersive spectrometer (HORIBA EX-250). The surface chemical states and elemental composition were analyzed by X-ray photoelectron spectroscopy (XPS, Thermo Escalab 250Xi, Al Kα radiation source). All binding energies were calibrated using the C 1s peak (284.8 eV) as a reference, with a calibration accuracy of ±0.2 eV. Raman spectra were collected on a Renishaw inVia spectrometer (excitation wavelength 532 nm). Ultraviolet-visible diffuse reflectance spectra (UV-vis DRS) were measured using a Shimadzu UV-3600 spectrometer equipped with an integrating sphere, with $BaSO_4$ used as a reflectance standard. Photoluminescence (PL) spectra were recorded on an FLS1000 spectrofluorometer (UK) with excitation wavelengths of 380 nm and 460 nm, respectively.

Catalytic performance testing

The CO_2 methanation performance test was conducted in an atmospheric pressure fixed-bed reactor system (PFD-5000), which has both thermal and photocatalytic functions. The reactor used a flat-wall quartz tube (length 400 mm, inner diameter 3 mm), with the catalyst bed located in its central region, measuring 3 × 14 × 14 mm. For the photothermal test, 150 mg of catalyst was loaded onto quartz wool. The reaction temperature was monitored in real-time by a K-type thermocouple placed beside the bed. Light irradiation was provided by a 300 W xenon lamp (PLS-SXE300) through an integrated quartz window. Before the reaction, the catalyst was subjected to *in situ* reduction under a H_2 atmosphere (flow rate 60 mL min^{-1}) for 2 hours, and then cooled to 150 °C under a N_2 atmosphere. Catalytic performance evaluation was carried out under atmospheric pressure in the temperature range of 150–400 °C. The reaction gas mixture had a composition of $H_2:CO_2:N_2$ (volume ratio 74.5 : 18.0 : 7.5), with a total flow rate of 60 mL min^{-1} (gas hourly space velocity, GHSV = 24 000 mL g^{-1} h^{-1}). The effluent gas was first subjected to dehumidification pretreatment and then analyzed using a GC97Plus gas chromatograph equipped with a thermal

conductivity detector (TCD) and a flame ionization detector (FID), using a TDX-01 column to ensure accurate component separation and detection. Aqueous by-products generated during the reaction stage were removed *via* a bottom drainage device.

The CO_2 conversion, CH_4 selectivity and CH_4 space–time yield for photothermal CO_2 methanation were calculated using the following equations:

$$X_{CO_2} = \frac{N_{CO_2,in} - N_{CO_2,out}}{N_{CO_2,in}} \times 100\%$$

$$S_{CH_4} = \frac{N_{CH_4,out}}{N_{CO_2,in} - N_{CO_2,out}} \times 100\%$$

$$STY_{CH_4} = \frac{WHSV \times X_{CO_2} \times S_{CH_4} \times nCO_2}{22.4}$$

where: X_{CO_2} represents the CO_2 conversion; S_{CH_4} represents the CH_4 selectivity; STY_{CH_4} represents the space–time yield of CH_4 (mmol g_{cat}^{-1} h^{-1}); $N_{CH_4,out}$ represents the mole fraction of CH_4 in the outlet gas; $N_{CO_2,in}$ and $N_{CO_2,out}$ represent the mole fractions of CO_2 in the inlet and outlet gases, respectively; nCO_2 is the mole fraction of carbon dioxide in the reaction mixture.

The apparent activation energy (E_a) for the reaction was determined based on the Arrhenius equation:

$$\ln r_{CO_2} = \frac{F_{CO_2} \times X_{CO_2}}{m_{cat}} + \ln A$$

$$\ln r_{CO_2} = \frac{-E_a}{(R \cdot T)} + \ln A$$

The variables in the equations are defined as follows: rCO_2 represents the CO_2 reaction rate (mol g_{cat}^{-1} s^{-1}); m_{cat} represents the catalyst mass (g); R represents the molar gas constant (8.314 J mol^{-1} K^{-1}); A represents the pre-exponential factor; T represents the measured catalyst bed temperature (K); E_a is the apparent activation energy (J mol^{-1}).

Temperature-programmed desorption (TPD)

CO_2-TPD experiments were performed using a Quantachrome Chembet Pulsar TPD chemisorption analyzer. The catalyst was heated in a He flow (30 mL min^{-1}) to 400 °C at a rate of 10 °C min^{-1} and then cooled to 50 °C. Subsequently, a 10% CO_2/He mixture flow (30 mL min^{-1}) was introduced to the catalyst bed at 50 °C for 1 hour. The sample was then purged with He (30 mL min^{-1}) at 50 °C for 1 hour. Finally, the sample was heated to 800 °C in a He atmosphere at a rate of 10 °C min^{-1}, and the outlet gas was detected by the TCD.

In situ diffuse reflectance infrared Fourier transform spectroscopy

In-situ diffuse reflectance infrared Fourier transform spectroscopy (DRIFTS) was employed to identify key intermediate species during the CO_2 methanation reaction under dark and light-assisted conditions. Measurements were conducted on a Bruker Tensor II spectrometer equipped with a Harrick high-temperature reaction cell, which was fitted with a ZnSe infrared window and a separate quartz window for illumination. Before data collection, a background spectrum was collected under an Ar flow at 100 °C, and this condition was maintained for 30 minutes to ensure a stable baseline. All sample spectra were collected in the range of 4000–1000 cm^{-1} with a resolution of 4 cm^{-1}, accumulating 100 scans per spectrum to achieve a high signal-to-noise ratio. To accurately compare the reaction pathways, tests under dark and light-assisted conditions were performed under strictly identical thermal conditions; the only difference was the activation of the light source system (consisting of a 300 W xenon lamp and an AM 1.5G filter) during the light-assisted tests. This design ensured that, under a constant temperature profile, the influence of different energy inputs (thermal energy *vs.* photothermal synergy) on the reaction intermediates could be directly discerned.

Results and discussion

Structural and morphological characterization

Fig. S1(a) and (c) show the SEM images of the $Ni/CeNiO_3$ catalyst, indicating that it is primarily composed of large, irregular blocky structures accompanied by a small number of smaller blocks. In contrast, the corresponding $Ni/CeNiO_{3-x}$ catalyst in Fig. S1(b) and (d), although also exhibiting a blocky morphology, clearly displays a greater number of finer blocks due to the additional $NaBH_4$ reduction treatment introduced during its preparation.

Fig. 1(a) and (d) present the TEM images of the $Ni/CeNiO_3$ and $Ni/CeNiO_{3-x}$ catalysts, respectively. A comparison reveals that the $Ni/CeNiO_3$ catalyst is relatively loose and non-uniform, whereas the $Ni/CeNiO_{3-x}$ catalyst exhibits a compact and uniform structure. The HRTEM results in

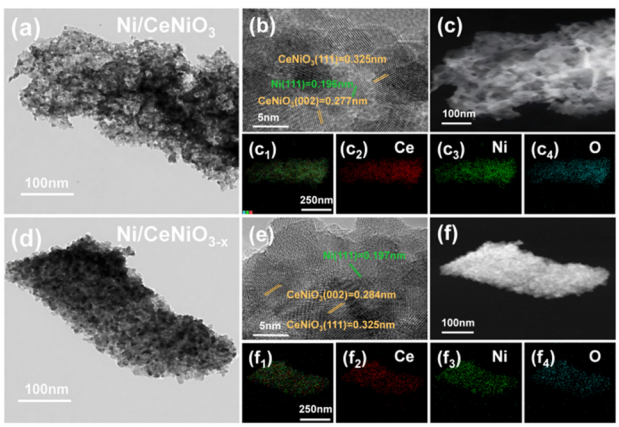

Fig. 1 Characterization results of $Ni/CeNiO_3$ and $Ni/CeNiO_{3-x}$ catalysts: (a and d) TEM images; (b and e) HRTEM images; (c and f) HAADF-STEM images; (c_1–c_4 and f_1–f_4) EDS elemental mapping images.

Fig. 1(b) and (e) show that regardless of $NaBH_4$ treatment, the exposed crystal facets of $CeNiO_3$ are predominantly (111) and (002), and the Ni particles also predominantly expose the (111) facet. This indicates that the introduction of NaBH4 did not alter the main exposed facets of the materials, thus ruling out potential influences of facet differences on catalytic reactivity. Furthermore, according to the EDS elemental mapping results (Fig. $1c_1$–c_4 and f_1–f_4), both catalysts demonstrate good elemental dispersion, suggesting that the $NaBH_4$ treatment did not significantly affect their elemental distribution.

Fig. S2(b) and (d) display the statistical results of Ni particle size distribution for the $Ni/CeNiO_3$ and $Ni/CeNiO_{3-x}$ catalysts, respectively. The $Ni/CeNiO_3$ catalyst has an average particle size of 6.90 nm, with particles mainly distributed in the range of 4.50–10.00 nm. In contrast, the average particle size of the $Ni/CeNiO_{3-x}$ catalyst increases to 8.58 nm, and its primary distribution range correspondingly shifts to 6.00–11.00 nm. It is noteworthy that the larger Ni particle size in $Ni/CeNiO_{3-x}$ is beneficial for the methanation reaction: excessively small Ni particles are prone to cause carbon deposition, leading to catalyst deactivation; conversely, a moderate increase in particle size helps suppress carbon deposition, thereby enabling the catalyst to maintain high activity levels.[18]

Fig. 2(a) shows the XRD patterns of $CeNiO_3$, $Ni/CeNiO_3$, and $Ni/CeNiO_{3-x}$. The diffraction peaks of $CeNiO_3$ at 2θ = 28.55°, 33.09°, 37.15°, 43.30°, 47.45°, 56.41°, 59.03°, 62.95°, 69.50°, 76.77°, and 79.16° correspond to the (111), (002), (112), (221), (040), (321), (123), (331), (331), (412), and (161) crystal planes, respectively,[19] which match the standard card for $CeNiO_3$ (ID: mp-776 207),[20] confirming its typical perovskite structure. After Ni exsolution, the patterns of $Ni/CeNiO_3$ and $Ni/CeNiO_{3-x}$ show characteristic peaks of metallic Ni at 44.51° and 52.01°, confirming the successful formation of Ni nanoparticles from the perovskite lattice. The persistence of a NiO diffraction peak at 43.30° indicates that part of the perovskite structure remains, with Ni existing in both metallic and oxidized states; thus, the designations $Ni/CeNiO_3$ and $Ni/CeNiO_{3-x}$ are appropriate. The introduction of sodium borohydride is accompanied by significant narrowing and sharpening of the diffraction peaks for $Ni/CeNiO_{3-x}$, corresponding to an increase in the crystallite size of the material, a change also confirmed by the particle size distribution results.

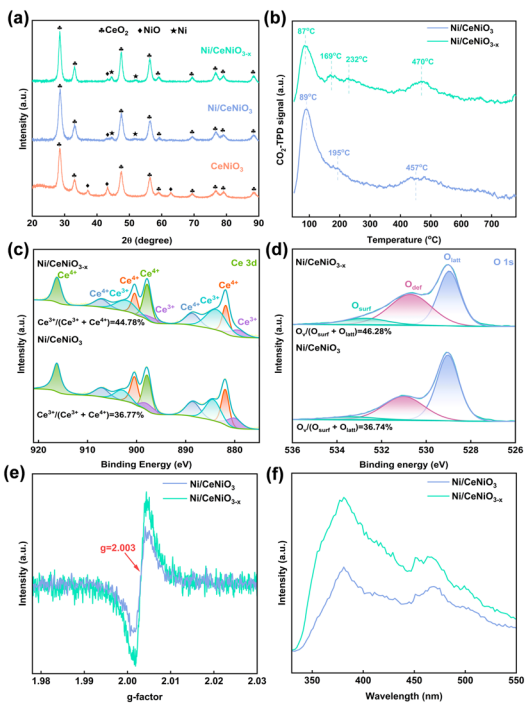

Fig. 2 Characterization results of $Ni/CeNiO_3$ and $Ni/CeNiO_{3-x}$ catalysts: (a) XRD images; (b) CO_2-TPD images; (c) Ce 3d; (d) O 1s; (e) EPR images; (f) PL images.

To further investigate the surface properties, CO_2-TPD tests were conducted on $Ni/CeNiO_3$ and $Ni/CeNiO_{3-x}$ to evaluate their basic site distribution (Fig. 2b). Based on the CO_2 desorption temperature, the basic sites can be classified into three types: weak (50–150 °C), medium (150–350 °C), and strong (350–600 °C) basic sites. $Ni/CeNiO_{3-x}$ exhibits fewer weak basic sites, indicating a higher concentration of oxygen vacancies.[21] The increase in oxygen vacancies weakens the weak adsorption of CO_2 while enhancing the number of medium-strength basic sites.[22] Medium-strength basic sites are particularly crucial for the CO_2 methanation reaction as they promote the moderate adsorption and activation of CO_2, thereby optimizing the reaction pathway.[23] $Ni/CeNiO_{3-x}$ clearly possesses a richer distribution of medium-strength basic sites, consistent with its superior catalytic performance. The appropriate weak/medium basic site adsorption on the $Ni/CeNiO_{3-x}$ catalyst helps weaken the C–O bond and facilitates product desorption, enabling CO_2 to react with dissociated H to form CH_4 *via* carbonate intermediates.[24,25]

Furthermore, as shown in Fig. S3, the reduction peaks in the ranges of 50–170 °C, 170–320 °C, and 360–540 °C correspond to the reduction of α-NiO, β-NiO, and γ-NiO, respectively. The narrower signal for β-NiO in $Ni/CeNiO_{3-x}$ compared to $Ni/CeNiO_3$ further confirms the higher concentration of oxygen vacancies in $Ni/CeNiO_{3-x}$.

A series of characterization tests were performed to investigate the presence and relative concentration of oxygen vacancies in the $Ni/CeNiO_3$ and $Ni/CeNiO_{3-x}$ catalysts. As shown in the Ce 3d spectra (Fig. 2c),[25,26] the $Ni/CeNiO_{3-x}$ catalyst exhibits a significantly higher proportion of Ce^{3+}. The $Ce^{3+}/(Ce^{3+} + Ce^{4+})$ ratio increases from 36.77% in $Ni/CeNiO_3$ to 44.78% in $Ni/CeNiO_{3-x}$. This notable increase confirms a higher concentration of oxygen vacancies on the surface of the $Ni/CeNiO_{3-x}$ catalyst. Additionally, the O 1s spectra (Fig. 2d)[21] show that the proportion of oxygen vacancies, represented by $O_v/(O_{surf} + O_{latt})$, is 36.74% in $Ni/CeNiO_3$ and increases to 46.28% in $Ni/CeNiO_{3-x}$, further verifying the increased number of surface oxygen vacancies.

To directly compare the oxygen vacancy concentration between the two catalysts, electron paramagnetic resonance (EPR) tests were conducted. The results, shown in Fig. 2(e), reveal a pair of sharp, symmetric signals at g = 2.003. This signal is associated with electrons trapped at defect sites and is generally considered characteristic evidence for the presence of oxygen vacancies.[27,28] Compared to Ni/CeNiO$_3$, Ni/CeNiO$_{3-x}$ displays a stronger EPR signal, indicating a higher concentration of electron trapping centers (oxygen vacancies), further confirming the oxygen vacancy enrichment suggested by XPS.

The enhanced photoluminescence (PL) intensity of Ni/CeNiO$_{3-x}$ within the 320–500 nm range (Fig. 2f) directly indicates a higher concentration of oxygen vacancies in its bulk phase, consistent with XPS and EPR results. These oxygen vacancies act as radiative recombination centers, leading to the observed PL enhancement.

The apparent contradiction between the stronger PL signal and the superior photocurrent response of Ni/CeNiO$_{3-x}$ (Fig. 3c) can be explained by a synergistic mechanism involving the oxygen vacancies and the Ni–CeO$_2$ Schottky junction. Specifically, the bulk oxygen vacancies first serve as electron traps, effectively capturing photogenerated electrons and delaying bulk recombination (reflected in the PL change). Subsequently, the built-in electric field of the Schottky junction drives the directional migration of these trapped electrons to the surface of Ni nanoparticles for participation in reactions (manifested as enhanced photocurrent and lower charge-transfer resistance, Fig. 3e). Therefore, the cooperative design of bulk defects (oxygen

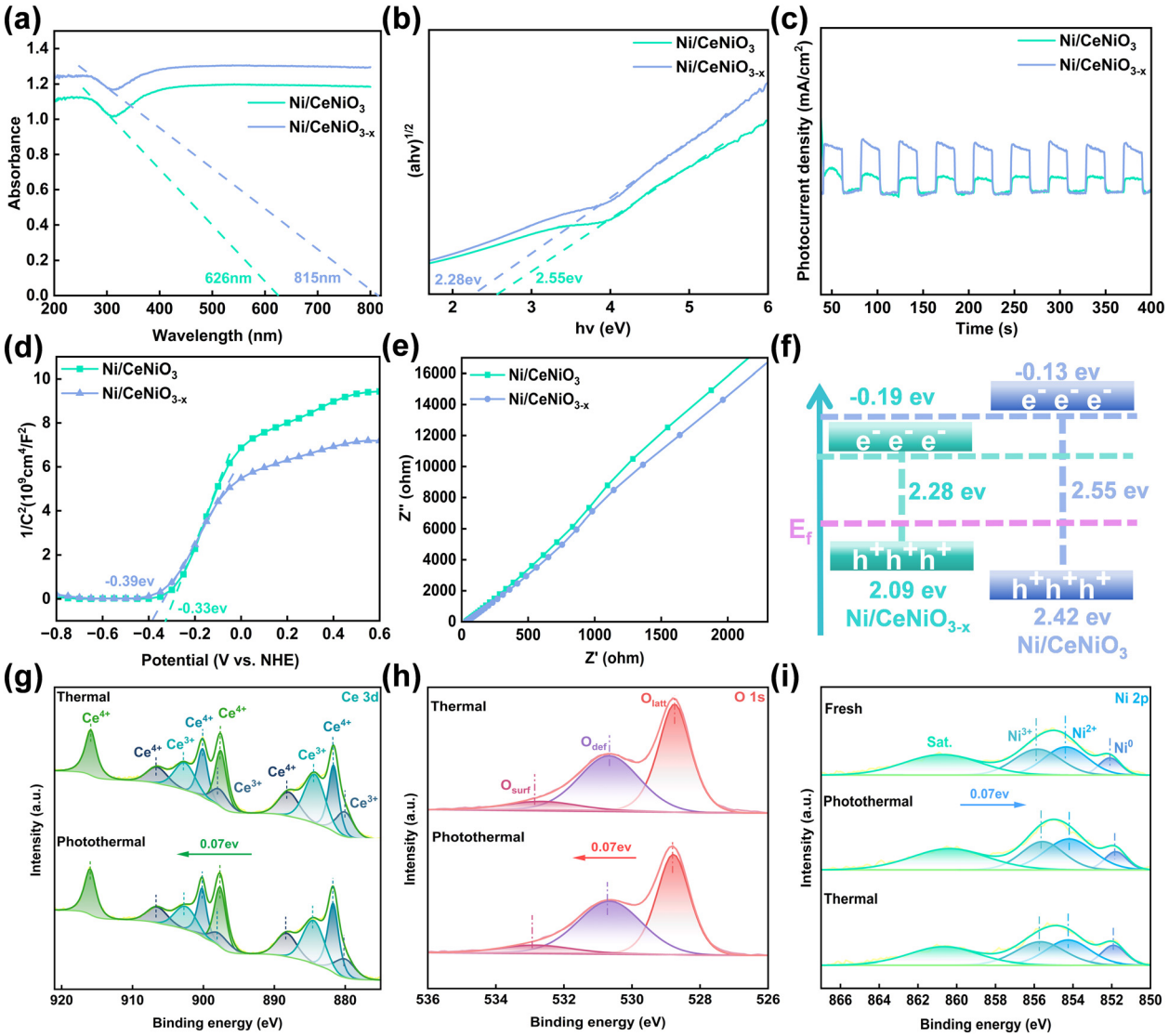

Fig. 3 Optical and photoelectrochemical characterization of Ni/CeNiO$_3$ and Ni/CeNiO$_{3-x}$ catalysts: (a) UV-vis absorption spectra; (b) Tauc plots; (c) transient photocurrent response curves; (d) Mott–Schottky plots; (e) electrochemical impedance spectra (EIS); (f) schematic diagram of conduction band (CB), valence band (VB), and Fermi level (E_f) positions (unit: eV); XPS spectra of the Ni/CeNiO$_{3-x}$ catalyst: (g) Ce 3d; (h) O 1s; (i) Ni 2p. Thermal: catalyst after the methanation reaction for 4 h under purely thermal conditions at 250 °C without light irradiation; photothermal: catalyst after the methanation reaction for 4 h under light irradiation at 250 °C; fresh: after 2 h H$_2$ treatment unreacted catalyst.

vacancies) and interfacial structure (Schottky junction) collectively enables efficient separation and utilization of photogenerated charge carriers, which is key to the improved optoelectronic and photothermal performance.

The origin of enhanced photo-thermal catalytic performance

To investigate the influence of oxygen vacancies on the optical properties of the materials, a series of characterizations were performed on the two catalysts. Fig. 3(a) shows the UV-vis spectra of $Ni/CeNiO_3$ and $Ni/CeNiO_{3-x}$, indicating that both exhibit full absorption characteristics in the ultraviolet-visible range.[29] Notably, $Ni/CeNiO_{3-x}$, with more oxygen vacancies, demonstrates stronger light absorption capacity, suggesting higher light utilization efficiency, which is conducive to generating more photogenerated carriers and thereby enhancing photocatalytic performance. The band gaps calculated using the Kubelka–Munk function $(\alpha h\nu)^n = A(h\nu - E_g)$[29] are shown in Fig. 3(b): 2.55 eV for $Ni/CeNiO_3$ and 2.28 eV for $Ni/CeNiO_{3-x}$. The introduction of an oxygen-vacancy-rich structure significantly narrows the band gap, reducing the energy required for photogenerated electrons to transition from the valence band to the conduction band, which favors an increase in carrier concentration.

The transient photocurrent response curves in Fig. 3(c) show that both catalysts exhibit good reproducibility and stability over multiple on–off light cycles. However, $Ni/CeNiO_{3-x}$ displays a significantly stronger photocurrent response, indicating higher mobility and a lower recombination rate of its photogenerated carriers.[30] The flat-band potentials (EFB) measured relative to NHE *via* Mott–Schottky tests (Fig. 3d) at pH = 7 are −0.33 eV for $Ni/CeNiO_3$ and −0.39 eV for $Ni/CeNiO_{3-x}$. The negative slopes confirm that both are n-type semiconductors. Using the relationship $E_{NHE} = E_{Ag/AgCl} + 0.197$ V, their conduction band potentials (E_{CB}) are derived as −0.13 eV and −0.19 eV, respectively. The valence band potentials (E_{VB}), calculated *via* $E_{VB} = E_g + E_{CB}$, are 2.42 eV and 2.09 eV, respectively. The schematic diagram of the energy band structure (Fig. 3f) shows a clearly narrowed band gap for $Ni/CeNiO_{3-x}$, primarily attributed to the defect energy levels introduced by oxygen-vacancy-rich defects. The reduced band gap enhances the material's photon absorption capacity and electron transition efficiency, thereby significantly boosting photocatalytic activity. Furthermore, the electrochemical impedance spectra (Nyquist plots, Fig. 3e) show that $Ni/CeNiO_{3-x}$ has a smaller arc radius, indicating lower charge transfer resistance, enhanced interfacial charge transfer capability, and superior electrical conductivity, all of which contribute to further improving the catalytic reaction activity.

Systematic characterization demonstrates that the introduction of the oxygen-vacancy-rich structure significantly modulates the electronic structure and optical properties of the $Ni/CeNiO_{3-x}$ catalyst. The narrowed band gap, enhanced light absorption, and improved carrier separation and transport efficiency collectively contribute to the enhanced photocatalytic performance. XPS technology was employed to analyze the surface elemental composition and chemical states of the $Ni/CeNiO_{3-x}$ catalyst after the thermal reaction and photothermal reaction. In the Ce 3d and O 1s XPS spectra shown in Fig. 3(g) and (h), compared to the sample after the pure thermal reaction, the binding energies of both the Ce 3d and O 1s orbitals in the catalyst subjected to the photothermal reaction shifted by 0.07 eV towards higher binding energy (Table S1). Conversely, in the Ni 2p spectrum shown in Fig. 3(i), the binding energy after the photothermal reaction shifted by 0.07 eV towards lower binding energy (Table S1). This opposing shift trend indicates the presence of a Schottky junction at the interface between the CeO_2 support and the metallic Ni.[31] This potential barrier can facilitate the unidirectional migration of photogenerated electrons from the conduction band of CeO_2 to the adjacent Ni nanoparticles (NPs) under light excitation, thereby effectively suppressing electron–hole recombination and enhancing the separation and utilization efficiency of photogenerated carriers.[16] Simultaneously, this process increases the electron density on the Ni surface, helping to maintain its metallic state (Ni^0), which significantly enhances the catalytic performance in the photothermal methanation reaction.[32,33]

Further analysis of the valence state of the Ni element before and after the reaction (Table S2) revealed that the content of Ni^0 in the fresh catalyst was 15.22%, which decreased to 14.49% after the thermal reaction, indicating that Ni^0 serves as the active center for the methanation reaction. After the photothermal reaction, the Ni^0 content was maintained at 15.30%. This result confirms that during the photothermal reaction, there is a transfer of photogenerated electrons from the support to Ni, effectively maintaining the Ni^0 valence state, thereby promoting the enhancement of the photothermal methanation catalytic performance.[34]

In summary, the oxygen vacancies in $Ni/CeNiO_{3-x}$ play a dual yet sequential role in managing photogenerated electrons. Primarily, they act as efficient trapping centers that instantaneously localize hot carriers upon photoexcitation, thereby suppressing bulk recombination and concurrently enhancing CO_2 adsorption and activation through increased local electron density. Subsequently, these trapped electrons are not permanently immobilized; instead, the defect bands associated with oxygen vacancies serve as hopping channels, facilitating the migration of electrons towards the Ni–CeO_2 interface. There, the built-in electric field of the Schottky junction provides a directional force, efficiently injecting electrons into Ni nanoparticles for the surface hydrogenation reactions. The optimal photocatalytic performance is achieved by balancing these two functions—ensuring sufficient traps for charge separation and activation, while maintaining a percolation pathway for efficient interfacial

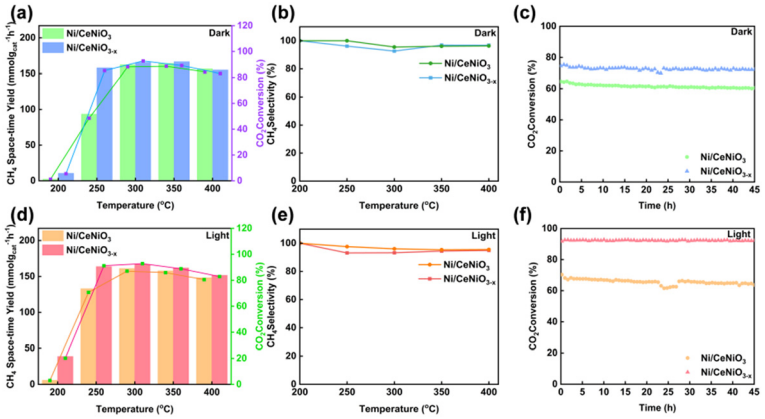

Fig. 4 Methanation activity of $Ni/CeNiO_3$ and $Ni/CeNiO_{3-x}$ catalysts under dark (thermal) and light (photothermal) conditions: (a and d) CH_4 space–time yield and CO_2 conversion rate; (b and e) CH_4 selectivity; (c and f) $Ni/CeNiO_3$ and $Ni/CeNiO_{3-x}$ stability test at 250 °C under light and dark conditions for 40 h.

transfer, as realized by the moderate concentration of oxygen vacancies introduced *via* the $NaBH_4$ treatment.

Performance testing of catalysts

The CO_2 methanation performance of $Ni/CeNiO_3$ and $Ni/CeNiO_{3-x}$ catalysts under both photothermal and purely thermal conditions was investigated within the temperature range of 200–400 °C. The results are shown in Fig. 4(a) and (d). Under purely thermal conditions, the performance difference between the two catalysts was most significant at 250 °C: $Ni/CeNiO_3$ exhibited a CH_4 generation rate of 93.6 mmol g^{-1} h^{-1}, a CO_2 conversion of 48.5%, and 100% CH_4 selectivity; whereas $Ni/CeNiO_{3-x}$ demonstrated a significantly higher CH_4 generation rate of 158.0 mmol g^{-1} h^{-1}, a CO_2 conversion of 85.2%, and a CH_4 selectivity of 96.2%. The dramatic activity difference under purely thermal conditions (where photocarriers are absent) cannot be rationalized by the moderate increase in Ni particle size alone, strongly indicating that the altered surface chemistry (*i.e.*, enriched oxygen vacancies) is the primary contributor to the enhanced intrinsic activity.

Under photothermal conditions, the performance of both catalysts was further improved. The CH_4 generation rate of $Ni/CeNiO_3$ at 200 °C increased from 2.3 mmol g^{-1} h^{-1} under pure thermal conditions to 5.9 mmol g^{-1} h^{-1}; under the same temperature, that of $Ni/CeNiO_{3-x}$ increased markedly from 10.5 mmol g^{-1} h^{-1} to 38.9 mmol g^{-1} h^{-1}. The performance enhancement under light illumination was more pronounced for the oxygen-vacancy-rich $Ni/CeNiO_{3-x}$ catalyst in the low-temperature region. The most significant performance difference remained at 250 °C under photothermal conditions: $Ni/CeNiO_3$ achieved a CH_4 generation rate of 133.0 mmol g^{-1} h^{-1}, a CO_2 conversion of 70.6%, and a CH_4 selectivity of 97.6%; while $Ni/CeNiO_{3-x}$ reached a CH_4 generation rate of 163.7 mmol g^{-1} h^{-1}, a CO_2 conversion of 91.2%, and a CH_4 selectivity of 93.1%. Notably, under light illumination, $Ni/CeNiO_{3-x}$ exhibited a higher CH_4 yield than $Ni/CeNiO_3$ at all tested temperatures, which originates from its oxygen-vacancy-rich structure effectively suppressing electron–hole recombination and improving carrier separation efficiency, thereby enhancing the activity of the methanation reaction.[35]

Further analysis of the reaction kinetics *via* Arrhenius plots (Fig. S4) revealed that light illumination significantly reduced the apparent activation energy. The activation energy for $Ni/CeNiO_3$ decreased from 11.47 to 5.82 kJ mol^{-1} under pure thermal conditions, while for $Ni/CeNiO_{3-x}$, it decreased from 11.14 to 4.07 kJ mol^{-1} under photothermal conditions. These results indicate that light illumination not only promotes the catalytic reaction rate but also likely involves the participation of photogenerated electrons in the CO_2 methanation process, thereby effectively lowering the reaction energy barrier. To evaluate the stability of the $Ni/CeNiO_3$ and $Ni/CeNiO_{3-x}$ catalysts, their methanation performance was tested at 250 °C. As shown in Fig. 4(c) and (f), the $Ni/CeNiO_{3-x}$ catalyst demonstrated superior and more stable catalytic performance compared to the $Ni/CeNiO_3$ catalyst, under both light and dark conditions. The improved stability of $Ni/CeNiO_{3-x}$ may benefit from the combined effects of strengthened metal–support interaction (due to oxygen vacancies) and the optimized Ni particle size.

Furthermore, a comparison with recent Ni-based catalysts (Table 1) shows that the $Ni/CeNiO_{3-x}$ catalyst in this study possesses excellent catalytic performance, ranking among the best in terms of activity.

To assess the potential impact of photothermal heating effects, systematic temperature monitoring was conducted. As shown in Table S3, the temperature increase of the reaction system under light illumination was extremely limited, with a maximum rise not exceeding 5 °C. This result indicates that the thermal fluctuations induced by light illumination are within a very limited range, and therefore can be considered negligible in this study.

Table 1 Performance comparison with various catalysts

Catalysts	Reaction process	Temperature (°C)	Reaction conditions		X_{CO_2} (%)	S_{CH_4} (%)	Ref.
			$CO_2:H_2$	WHSV (mL g^{-1} h^{-1})			
Ni/ZrO_{2-x}	Thermal catalysis	230	1 : 4	30 000	~72	~100	36
$NiCe\text{-}600H_2$	Thermal catalysis	275	1 : 4	~12 000	~25	~93	37
$Ni/La_2O_3–CeO_2/ZrO_2$	Thermal catalysis	250	1 : 4	15 000	~80	100	23
$Ni/CaTiO_3$	Photothermal catalysis	230	1 : 4	~6000	87.8	99.8	38
$Ni/SrTiO_{3-x}$	Photothermal catalysis	250	1 : 4	26 000	78	90	10
$Ni/0.5\text{-}TiO_2@NC$	Photothermal catalysis	275	1 : 4	~13 000	71.6	99.6	8
Ni/TiO_2	Photothermal catalysis	325	1 : 4	26 000	50.6	100	39
Ni/CeO_2	Photothermal catalysis	250	—	14 250	~39	—	40
$Ni/CeNiO_3$	Photothermal catalysis	250	1 : 4	24 000	70.6	97.6	This work
$Ni/CeNiO_{3-x}$	Photothermal catalysis	250	1 : 4	24 000	91.2	93.1	This work

To summarize, oxygen vacancies play distinct yet interconnected roles under thermal and photothermal conditions. Under thermal catalysis, they primarily function as highly active sites for CO_2 chemisorption and activation, lowering the kinetic barrier for the hydrogenation reaction and enhancing the intrinsic activity. Under photothermal catalysis, beyond their thermal catalytic function, the oxygen vacancies critically serve as effective electron traps and transfer mediators. They narrow the band gap for improved light harvesting, facilitate the separation of photogenerated carriers, and synergize with the Schottky junction to direct electrons toward Ni active sites, thereby realizing a remarkable photo-thermal synergy. Across both conditions, the oxygen vacancies contribute to superior stability by strengthening the metal–support interaction to resist sintering and, in the photothermal case, by helping maintain the metallic state of Ni through continuous electron supply.

Research on the mechanism of catalysts

The reaction mechanism of syngas conversion catalyzed by $Ni/CeNiO_3$ and $Ni/CeNiO_{3-x}$ under thermal and photothermal conditions was systematically investigated using *in situ* FTIR technology. As shown in Fig. 5(a), under thermal conditions, signals for species such as m-HCOO (1582 cm^{-1}),[41] m-CO_3^{2-} (1511 cm^{-1}),[42,43] and b-CO_3^{2-} (1372 cm^{-1})[44] began to appear for $Ni/CeNiO_3$ after introducing syngas at 150 °C. As the temperature increased, the intensities of these bands were

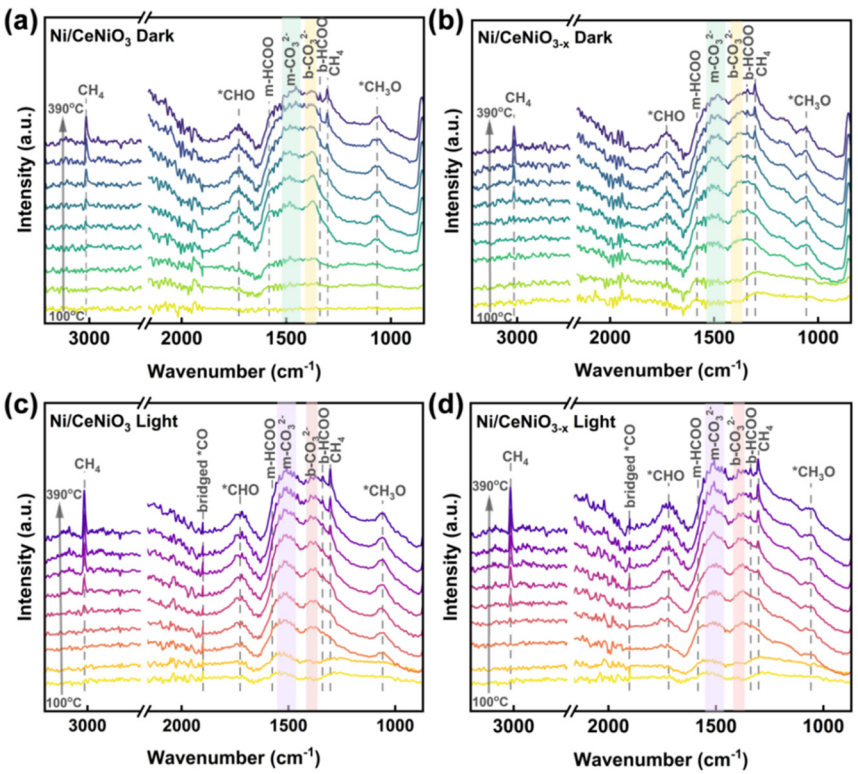

Fig. 5 The *in situ* FTIR spectra of the catalysts under both dark (thermal) and light (photothermal) conditions: (a and c) $Ni/CeNiO_3$; (b and d) $Ni/CeNiO_{3-x}$.

gradually enhanced. Among them, m-HCOO and b-CO_3^{2-} reached their maximum intensities at 240 °C and then began to decrease, indicating their role as key reaction intermediates participating in subsequent steps. Simultaneously, distinct bands for *CHO (1726 cm^{-1})[45] and *CH_3O (1066 cm^{-1})[46] appeared at 240 °C, accompanied by the formation of b-HCOO (1339 cm^{-1}),[47] further suggesting that the formate intermediate primarily exists in the monodentate configuration (m-HCOO) rather than the bidentate configuration (b-HCOO). When the temperature was raised to 270 °C, characteristic absorption peaks of CH_4 (3015 cm^{-1} and 1302 cm^{-1})[38,47] were observed, and their intensity continued to increase with further temperature rise.

In the thermal condition experiment for Ni/$CeNiO_{3-x}$ shown in Fig. 5(b), m-HCOO, m-CO_3^{2-}, and b-CO_3^{2-} began to appear at a lower temperature (100 °C). Furthermore, m-HCOO and b-CO_3^{2-} reached their peak intensities at 210 °C and were subsequently converted to CHO and CH_3O. However, CH_4 generation still commenced at 270 °C, indicating that although oxygen vacancies promote the conversion of intermediates, the energy barrier for the CH_4 formation step requires additional energy input to lower the reaction temperature. The comparison between the two catalysts under thermal conditions demonstrates that increasing the oxygen vacancy concentration effectively accelerates the conversion of key intermediates. Under photothermal conditions (Fig. 5(c) and (d)), both Ni/$CeNiO_3$ and Ni/$CeNiO_{3-x}$ exhibited significantly enhanced catalytic behavior. Light illumination caused all intermediate species (including m-HCOO, m-CO_3^{2-}, and CO_3^{2-}), as well as bridged CO (ref. 45 and 48) and CHO, to appear simultaneously at 100 °C. The early formation of *CHO further promoted the premature generation of CH_4. At 210 °C, concomitant with m-HCOO and b-CO_3^{2-} reaching their peak intensities, *CH_3O and CH_4 also began to form. Moreover, the CH_4 signal was stronger on the oxygen-vacancy-rich Ni/$CeNiO_{3-x}$, indicating a higher methane yield.

Both catalysts under thermal and photothermal conditions followed the reaction path: CO_2 → b-CO_3^{2-} → m-HCOO → *CHO→ *CH_2O → *CH_3O → CH_4. However, compared to purely thermal catalytic conditions, photothermal conditions lowered the CH_4 formation temperature by 60 °C and significantly enhanced the intensity of its characteristic peaks. This indicates that the photo-induced effect effectively promotes the formation of intermediates like m-HCOO and the subsequent hydrogenation steps without altering the fundamental reaction pathway.

The dramatic 60 °C decrease in the CH_4 formation temperature under illumination, as evidenced by *in situ* DRIFTS (Fig. 5), suggests a selective photo-promotion effect on a specific elementary step. By comparing the evolution sequences under thermal and photothermal conditions (Fig. 5b *vs.* d), it is evident that the formation of the *CHO intermediate (1726 cm^{-1}) is most strongly accelerated. Under thermal conditions, *CHO appears only after m-HCOO reaches its maximum intensity at 210 °C. In stark contrast, under illumination, *CHO and m-HCOO emerge simultaneously at temperatures as low as 100 °C and grow concurrently. This indicates that the photogenerated electrons, efficiently delivered to the Ni–CeO_{2-x} interface *via* the Schottky junction and trapped by oxygen vacancies, predominantly lower the activation barrier for the hydrogenative C–O bond cleavage of m-HCOO to form *CHO. The early and abundant supply of CHO then cascades forward, enabling the subsequent hydrogenation steps (CHO → *CH_3O → CH_4) to proceed at significantly lower overall temperatures.

In summary, oxygen vacancies play distinct yet interconnected roles under thermal and photothermal conditions. The more rapid conversion of intermediates for oxygen-vacancy-rich Ni/$CeNiO_{3-x}$ under thermal conditions and the stronger CH_4 peaks under photothermal conditions suggest that the oxygen-vacancy-rich catalyst facilitates the adsorption of more CO_2 and the formation of b-CO_3^{2-} species, thereby promoting CO_2 hydrogenation and activation. Meanwhile, photothermal conditions enhance the interfacial electron transfer efficiency, effectively lowering the barrier for CH_4 formation. The synergistic effect between these two factors effectively overcomes the kinetic limitations of single energy input modes, enabling highly efficient low-temperature methane synthesis under atmospheric pressure.

Conclusion

This study successfully constructed a Ni/$CeNiO_{3-x}$ catalyst with a Schottky junction structure by regulating the oxygen vacancy concentration in the $CeNiO_3$ precursor, and systematically investigated its performance and mechanism in the photothermal catalytic CO_2 methanation reaction. Structural characterization and photoelectrochemical performance tests revealed that the introduction of the oxygen-vacancy-rich structure effectively narrows the material band gap, enhances light absorption capacity, and improves carrier separation efficiency. The Schottky junction formed at the interface between Ni and the CeO_2 support promotes the unidirectional migration of electrons, significantly suppressing the recombination of photogenerated carriers. Catalytic performance tests demonstrated that Ni/$CeNiO_{3-x}$ exhibits excellent low-temperature activity and stability under photothermal conditions, achieving a CH_4 production rate as high as 163.7 mmol g^{-1} h^{-1} at 250 °C, CO_2 a conversion rate of 91.2% and a CH_4 selectivity of 93.1%, highlighting its application potential in low-temperature photothermal catalytic reactions. *In situ* infrared spectroscopy further elucidated the reaction mechanism whereby CO_2 is efficiently converted to CH_4 *via* carbonate and formate intermediate pathways.

Conflicts of interest

There are no conflicts to declare.

Data availability

All experimental data, characterization results, and analysis files that support the conclusions of this work are provided in the main text and supplementary information (SI). Raw datasets, including XRD patterns, TEM characterization, UV-vis spectra, PL spectra, XPS spectra, DRIFTS profiles, and catalytic performance data, are available from the corresponding author upon reasonable request. The data supporting the graphical figures and tables in this article have been archived and can be made accessible for verification and reuse purposes. Supplementary information: SEM; particle size distribution; H_2-TPR; Arrhenius plots; stability tests. See DOI: https://doi.org/10.1039/d5cy01413a.

Acknowledgements

This work was financially supported by Xinjiang Science and Technology Program (No. 2023TSYCCX0118).

References

1 H. Kong, C. Xing, C. Liu, Z. Chen, L. Zhao, W. Gao, H. Liu, K. Song, C. Li, L. Wang and W. Zhou, *Adv. Energy Mater.*, 2025, e03113.
2 Y. F. Zhu, B. Xie, J. A. Yuwono, P. Kumar, A. S. Sharma, M. P. Nielsen, A. Bendavid, R. Amal, J. Scott and E. C. Lovell, *EES Catal.*, 2024, **2**, 834–849.
3 F. Rathmann, I. Abdelsalam, S. Wang, A. Reznichenko, M. Reinikainen and P. H. C. Camargo, *ACS Appl. Energy Mater.*, 2025, **8**, 8365–8375.
4 Z. Xia, J. Zhai, L. Lin, X. Chen, C. Xue, S. Jia, J. Jiao, M. Dong, W. Han, X. Zheng, T. Xue, H. Wu and B. Han, *Chem. Sci.*, 2025, **16**, 13382–13389.
5 T. West, *Nat. Synth.*, 2023, **2**, 707.
6 Z.-H. He, Z.-H. Li, Z.-Y. Wang, K. Wang, Y.-C. Sun, S.-W. Wang, W.-T. Wang, Y. Yang and Z.-T. Liu, *Green Chem.*, 2021, **23**, 5775–5785.
7 S. Chen, A. M. Abdel-Mageed, M. Dyballa, M. Parlinska-Wojtan, J. Bansmann, S. Pollastri, L. Olivi, G. Aquilanti and R. J. Behm, *Angew. Chem., Int. Ed.*, 2020, **59**, 22763–22770.
8 Z. Xiao, P. Li, H. Zhang, S. Zhang, Y. Zhao, J. Gu, Z. Lian, G. Li, J.-J. Zou and D. Wang, *J. Colloid Interface Sci.*, 2024, **672**, 642–653.
9 C. Vogt, M. Monai, G. J. Kramer and B. M. Weckhuysen, *Nat. Catal.*, 2019, **2**, 188–197.
10 H. Li, Y. Tang, W. Yan, M. Liu, Z. Wang, J. Li and F. Yu, *Appl. Catal., B*, 2024, **357**, 124346.
11 X. Yu, X. Ding, Y. Yao, W. Gao, C. Wang, C. Wu, C. Wu, B. Wang, L. Wang and Z. Zou, *Adv. Mater.*, 2024, **36**, 2312942.
12 X. Zhang, J. Guo, L. Huang, S. Li, X. Zhou, Y. Zhang, Q. Xie, S. Mo, B. Li and J. Li, *Sep. Purif. Technol.*, 2024, **360**, 131047.
13 C. Guo, L. Wang, Y. Tang, Z. Yang, Y. Zhao, Y. Jiang, X. Wen and F. Wang, *Adv. Funct. Mater.*, 2024, **35**, 2414931.
14 J. Zhao, B. Liu, L. Meng, S. He, R. Yuan, Y. Hou, Z. Ding, H. Lin, Z. Zhang, X. Wang and J. Long, *Appl. Catal., B*, 2019, **256**, 117823.
15 X. Ma, S. Hou, D. Li, Y. Wu and S. Li, *Sep. Purif. Technol.*, 2024, **354**, 129057.
16 X. Guo, L. Fan, J. Liu, B. Wen, Y. Li and Z. Jin, *Appl. Catal., B*, 2025, **378**, 125586.
17 M. Sun, A. Sun, Q. Wu, H. Zhu, X. Liu and Y. Xing, *J. Mater. Sci. Technol.*, 2025, **255**, 86–95.
18 Y. Li, C. Shen, C. Jiang, C. Liang, B. Chen, W. Ding and X. Guo, *ACS Catal.*, 2025, **15**, 9728–9737.
19 X. Tang, H. Ding, Q. Han, G. Zhou, R. Ma, Z. Xue, S. Yan, L. Zhang, J. Yin and E. H. Ang, *Mater. Horiz.*, 2025, **12**, 8700–8710.
20 M. P. Harikrishnan, A. J. C. Mary and A. C. Bose, *Electrochim. Acta*, 2020, **362**, 137095.
21 H. Zhou, J. Yang, Y. Song, T. Geng, N. Zhao, Q. Wang, F. Xiao and J. Luo, *Adv. Funct. Mater.*, 2025, e25888.
22 X. Tang, C. Song, H. Li, W. Liu, X. Hu, Q. Chen, H. Lu, S. Yao, X.-n. Li and L. Lin, *Nat. Commun.*, 2024, **15**, 3115.
23 S. Li, G. Liu, S. Zhang, K. An, Z. Ma, L. Wang and Y. Liu, *J. Energy Chem.*, 2019, **43**, 155–164.
24 J. Ren, C. Mebrahtu, L. van Koppen, F. Martinovic, J. P. Hofmann, E. J. M. Hensen and R. Palkovits, *Chem. Eng. J.*, 2021, **426**, 131760.
25 T. Li, Z.-Y. Zhang, D.-C. Luo, B.-Y. Xu, R.-J. Zhang, J.-L. Yao, D. Li and T. Xie, *Nano Res.*, 2024, **17**, 7945–7956.
26 J. Xiangyang, C. Yishuang, Z. Peng, S. Shaojia, L. Jian and S. Weiyu, *Chin. Chem. Lett.*, 2025, **36**, 110719.
27 A. Shokrollahi, T. Hamoule and S. Sharifnia, *Fuel*, 2025, **404**, 135594.
28 Z. Li, D. Jia, W. Zhang, Y. Li, M. Wang and D. Zhang, *Front. Chem. Sci. Eng.*, 2024, **18**, 31.
29 M. Zhang, J. Wang, H. Xue, J. Zhang, S. Peng, X. Han, Y. Deng and W. Hu, *Angew. Chem., Int. Ed.*, 2020, **59**, 18463–18467.
30 S. Sun, X. Huang, X. Li, B. Wu, H. Liu, Z. Hua, T. Hou, A. Chen, S. Li, R. Shao and J. Zhang, *J. Mater. Chem. A*, 2025, **13**, 12397–12405.
31 S. Ning, Z. Chen, H. Huang, Z. Liu, Y. He, D. Wang, Y. Fan, C. X. Chen, M. Barboiu and C. Y. Su, *Small*, 2025, **21**, 2504721.
32 P. Shan, K. Geng, L. Guo, L. Kuang, Y. Shen, B. Xiong, J. Hou, F. Guo, G. Wang and W. Shi, *Chem. Eng. J.*, 2025, **513**, 162801.
33 Z. Rao, Y. Cao, Z. Huang, Z. Yin, W. Wan, M. Ma, Y. Wu, J. Wang, G. Yang, Y. Cui, Z. Gong and Y. Zhou, *ACS Catal.*, 2021, **11**, 4730–4738.
34 Q. M. Sun, J. J. Xu, F. F. Tao, W. Ye, C. Zhou, J. H. He and J. M. Lu, *Angew. Chem., Int. Ed.*, 2022, **61**, e202200872.
35 D. Zu, Y. Ying, Q. Wei, P. Xiong, M. S. Ahmed, Z. Lin, M. M. J. Li, M. Li, Z. Xu, G. Chen, L. Bai, S. She, Y. H. Tsang and H. Huang, *Angew. Chem., Int. Ed.*, 2024, **63**, e202405756.
36 H. Wang, Z. Li, G. Cui and M. Wei, *ACS Appl. Mater. Interfaces*, 2023, **15**, 19021–19031.
37 M. Barreau, D. Salusso, J. Zhang, M. Haevecker, D. Teschner, A. Efimenko, E. Borfecchia, K. Sobczak and S. Zafeiratos, *Small Sci.*, 2025, **5**, 2400540.
38 Z. Yuan, B. Zhang, X. Zhu, S. Wang, W. Sun, B. Huang, Z. Jiang, Y. Dai, Z. Wang, W. Wei, X. Tai and Y. Q. Lan, *Adv. Funct. Mater.*, 2025, **35**, 2503531.

39 P. Li, S. Zhang, Z. Xiao, H. Zhang, F. Ye, J. Gu, J. Wang, G. Li and D. Wang, *Fuel*, 2023, **357**, 129817.
40 Z. Yang, D. Zheng, X. Yue, K. Wang, Y. Hou, W. Dai and X. Fu, *Appl. Surf. Sci.*, 2023, **615**, 156311.
41 K. Wang, Y. Men, S. Liu, J. Wang, Y. Li, Y. Tang, Z. Li, W. An, X. Pan and L. Li, *Fuel*, 2021, **304**, 121388.
42 Q. Pan, J. Peng, T. Sun, S. Wang and S. Wang, *Catal. Commun.*, 2013, **45**, 74–78.
43 S. Ullah, S. M. Ahmed, T. Huang, Y. Pan, Z. Yu, Q. Xue, R. Ye, Z. Wang, S. Kawi, Y. Wang and G. Luo, *Chem. Eng. J.*, 2025, **515**, 163859.
44 A. Porta, R. Matarrese, C. G. Visconti and L. Lietti, *Energy Fuels*, 2023, **37**, 7280–7290.
45 Q. Ye, S. Li, Y. Liao, Y. Wang, Y. He, J. Chen, J. Xu, Q. Su and X. Cui, *Chem. Eng. J.*, 2024, **486**, 150426.
46 J. Fan, L. Shi, H. Ge, J. Liu, X. Deng, Z. Li and Q. Liang, *Adv. Funct. Mater.*, 2024, **35**, 2412078.
47 F. Hu, R. Ye, C. Jin, D. Liu, X. Chen, C. Li, K. H. Lim, G. Song, T. Wang, G. Feng, R. Zhang and S. Kawi, *Appl. Catal., B*, 2022, **317**, 121715.
48 J. Guo, J. Yang, Y. Song, W. Yan, S. Liu, J. Luo, N. Zhao and F. Xiao, *Chem. Eng. J.*, 2025, **522**, 167588.